Acta Pharmaceutica Sinica B 2025;15(5):2612–2624

Chinese Pharmaceutical Association
Institute of Materia Medica, Chinese Academy of Medical Sciences

Acta Pharmaceutica Sinica B

www.elsevier.com/locate/apsb
www.sciencedirect.com

ORIGINAL ARTICLE

First ATG101-recruiting small molecule degrader for selective CDK9 degradation *via* autophagy–lysosome pathway

Ye Zhong[a,†], Jing Xu[b,c,†], Huiying Cao[c], Jie Gao[c,e], Shaoyue Ding[a], Zhaohui Ren[c], Huali Yang[a], Yili Sun[c,d,*], Maosheng Cheng[a,*], Jia Li[b,c,d,*], Yang Liu[a,*]

[a]*Key Laboratory of Structure-Based Drug Design & Discovery, Ministry of Education, Shenyang Pharmaceutical University, Shenyang 110016, China*
[b]*Department of Pharmacology, Shenyang Pharmaceutical University, Shenyang 110016, China*
[c]*Shandong Laboratory of Yantai Drug Discovery, Bohai Rim Advanced Research Institute for Drug Discovery, Yantai 264117, China*
[d]*State Key Laboratory of Chemical Biology, Shanghai Institute of Materia Medica, Chinese Academy of Sciences, Shanghai 201203, China*
[e]*School of Pharmaceutical Science and Technology, Hangzhou Institute for Advanced Study, University of Chinese Academy of Sciences, Hangzhou 310024, China*

Received 24 November 2024; received in revised form 22 February 2025; accepted 5 March 2025

KEY WORDS

Protein degradation;
Hydrophobic tags;
ATG101;
Autophagy–lysosome pathway;
CDK9;
Cyclin T1;
Degrader;
Antitumor

Abstract Cyclin-dependent kinase 9 (CDK9) is a member of the transcription CDK subfamily and plays a role in transcriptional regulation. Selective CDK9 degraders possess potent clinical advantages over reversible CDK9 inhibitors. Herein, we report the first ATG101-recruiting selective CDK9 degrader, **AZ-9**, based on the hydrophobic tag kinesin degradation technology. **AZ-9** showed significant degradation effects and selectivity toward other homologous cell cycle CDKs *in vitro* and *in vivo*, which could also affect downstream related phenotypes. Mechanism research revealed that **AZ-9** recruits ATG101 to initiate the autophagy–lysosome pathway, and forms autophagosomes through the recruitment of LC3, which then fuses with lysosomes to degrade CDK9 and the partner protein Cyclin T1. These dates

*Corresponding authors.
E-mail addresses: yilisun@simm.ac.cn (Yili Sun), mscheng@syphu.edu.cn (Maosheng Cheng), jli@simm.ac.cn (Jia Li), y.liu@syphu.edu.cn (Yang Liu).
[†]These authors made equal contributions to this work.
Peer review under the responsibility of Chinese Pharmaceutical Association and Institute of Materia Medica, Chinese Academy of Medical Sciences.

https://doi.org/10.1016/j.apsb.2025.03.047

validated the existence of non-proteasomal degradation pathway of hydrophobic driven protein degradation strategy for the first time, which might provide research ideas for chemical induction intervention on other types of pathogenic proteins.

1. Introduction

As one of the representative targets of transcriptional regulation in CDK families, cyclin-dependent kinase 9 (CDK9) has attracted increasing attention as a clinically relevant target for addressing unsolved clinical needs, especially in tumors characterized by high transcriptional dependency[1-4]. To date, traditional small molecule CDK9 inhibitors, such as VIP152[5], AZD4573[6], KB0742[7], AT7519[8], SNS-032[9] (Supporting Information Fig. S1) et al., have not shown significant clinical advantages due to issues such as selectivity and toxicity. And the research on compounds that act on CDK9/Cyclin T1 protein−protein interaction (PPI) is still at the basic research stage[10-11], which has not been applied to clinical studies. Meanwhile, current CDK9 inhibitors are reversible and require continuous target occupancy to maintain the activity inhibition of CDK9. Thus, an urgent need exists for new strategies to ablate CDK9 activity potently and selectively.

Targeted protein degradation (TPD) technologies as a supplement to traditional target chemical intervention, which could eliminate related pathogenic factors by degrading proteins of interest (POIs)[12-15]. For CDK9, degradation could compensate to some extent for the weakness of reversible inhibitors that cannot sustain their effects, which could also provide a class of chemical probes to study the nonenzymatic function of CDK9. To date, we and others have developed several CDK9-related degraders in some reports[16-24].

However, previous reports only validated the degradation phenotype towards CDK9, without clearly elucidating the specific degradation mechanism and *in vivo* effectiveness. Moreover, the degradation selectivity of relevant CDK9 degraders still largely depends on the selectivity of the ligands used.

Recently, hydrophobic tag-based degraders have been reported to destabilize the protein of interest (POI) or mimic a partially unfolded protein state, which leads to degradation mediated by the recruitment of the endogenous chaperone protein (Hsp70 or Hsp90) or the proteasome[25-27]. Owing to their small molecular weight and increased number of druggable factors, hydrophobic tag-based degraders have become another popular research direction for degrading agents after PROTACs. However, the design principles and mechanisms of hydrophobic tag-based degraders for different POIs are still unable to form a system that can be summarized. Herein, in this work, we report the discovery of a first-in-class hydrophobic tag-based ATG101-recruiting selective CDK9 degrader **AZ-9**. Unlike previous reports, **AZ-9** activated the autophagy−lysosome degradation pathway to selectively degrade CDK9 by recruiting ATG101, a part of the autophagy initiator ULK complex. Importantly, **AZ-9** exhibits high CDK9 degradation selectivity and persistence both *in vitro* and *in vivo* over other cell cycle CDKs (CDK2, CDK4, and CDK6), suggesting that **AZ-9** might represent a useful lead compound tool for biological research related to CDK9 and clinical research on tumors with high transcriptional dependency.

2. Results and discussion

2.1. Discovery of *AZ-9* as potent CDK9 degrader

In this work, AT7519 was chosen as the binder of CDK9 for the design of novel degraders. As shown in Fig. 1A, AT7519 occupies the ATP-binding area of the CDK9/Cyclin T1 complex, and the secondary amine moiety on piperidine is exposed to the solvent region, offering a potential tethering site for the introduction of hydrophobic tags to become a signal for the recognition of incorrect proteins. We screened several hydrophobic moieties including 1,1-diyldibenzene, norbornene[28], ferrocene, adamantane[29-30] and *S*-indacene with linkers having lengths of four or five atoms (Fig. 1B). The HCT116 cell line (CDK9 high expression proved previously[31]) was chosen as the model to evaluate the degradation effects and cell inhibitory activity phenotype (**AZ-1**−**AZ-10**, the structures were listed in Supporting Information Fig. S2). The results reveal that the *S*-indacene moiety exposed to the surface of the CDK9/Cyclin T1 complex may cause increased degradation of CDK9 and Cyclin T1 (Fig. 1C and Supporting Information Fig. S4) together with increased antiproliferative activity (GI_{50} = 0.72 μmol/L). Furthermore, we retained the *S*-indacene moiety while modifying the length and properties of the linker (**AZ-11**−**AZ-13** listed in Supporting Information Fig. S3). Surprisingly, the degradation effects and cell inhibitory activities significantly decreased (Figs. S3 and S4), which suggest that the combination of *S*-indacene and the length of four atoms (**AZ-9**) extending out of CDK9/Cyclin T1 is relatively conserved.

2.2. *AZ-9* shows significant CDK9 degradation effects in HCT116 cells

To investigate the degradation phenotype of **AZ-9**, we first confirmed the DC_{50} of **AZ-9** in HCT116 cells. The results reveal that **AZ-9** could significantly degrade CDK9 and Cyclin T1 in a dose-dependent manner, with DC_{50} values of 0.4073 and 1.215 μmol/L, respectively (Fig. 2A−C). In the shCDK9 HCT116 model, **AZ-9** did not exhibit significant drug sensitivity characteristics when compared with the scramble control group ($GI_{50} > 10$ μmol/L, Fig. 2D and Supporting Information Fig. S5), suggesting that the inhibitory effect of **AZ-9** on HCT116 cells viability results from the degradation of CDK9 and Cyclin T1 rather than the inhibition of CDK9 or other targets. Furthermore, in HCT116 cells overexpressing CDK9, **AZ-9** still exhibited good degradation effects, which confirmed that the degradation effect of **AZ-9** on CDK9 was not affected by the protein concentration (Fig. 2E and F). We also investigated the degradation efficiency of CDK9 by **AZ-9** in HCT116 cells. As shown in Fig. 2G and H, **AZ-9** degraded CDK9 in a time-dependent manner in HCT116 cells as well, and significant degradation effects began to appear after 8 h. However, the content of Cyclin T1 did not

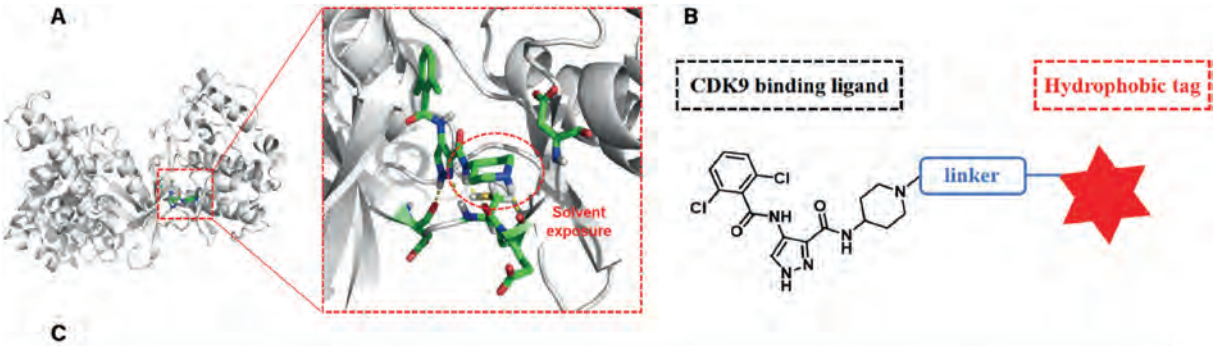

C

Cpd.	HCT116 cell line					Cpd.	HCT116 cell line				
	GI_{50}(μmol/L)	CDK9 degradation%		Cyclin T1 degradation%			GI_{50}(μmol/L)	CDK9 degradation%		Cyclin T1 degradation%	
		1	3	1	3			1	3	1	3
AZ-1	8.72±1.13	9.87	66.91	6.53	22.35	**AZ-6**	12.48±2.55	2.14	6.74	0.07	0.12
AZ-2	16.88±0.57	0.72	2.53	0.06	0.13	**AZ-7**	1.27±0.16	6.64	34.61	3.58	11.76
AZ-3	16.33±1.64	0.78	1.62	0.05	0.27	**AZ-8**	2.71±0.91	50.56	53.41	1.65	33.23
AZ-4	12.94±3.25	-18.31	-4.91	-11.5	-0.24	**AZ-9**	0.72±0.05	59.17	85.04	12.58	46.79
AZ-5	4.38±1.48	2.20	20.74	-1.12	0.36	**AZ-10**	2.52±1.03	30.59	69.49	7.64	35.80
AT7519 GI_{50} = 2.13±0.76 (μmol/L)											

Figure 1 Discovery of **AZ-9** as a potent CDK9 degrader. (A) Binding mode of AT7519 and CDK9/Cyclin T1 complex (PDB:4BCF); (B) Design strategy of CDK9 degraders based on hydrophobic tags; (C) Biological activities of **AZ-1**−**AZ-10**.

significantly decrease after 24 h of **AZ-9** exposure, suggesting that **AZ-9** has a faster degradation rate on proteins directly affected. To eliminate the influence of the half-life of intracellular CDK9, a CHX assay was performed, and the results revealed that within 8 h of inhibiting protein synthesis, there was no significant decrease in the content of CDK9, while the addition of **AZ-9** under the same conditions effectively reduced the content of CDK9 (Fig. 2I and J), suggesting that **AZ-9** chemically interferes with the degradation of CDK9 rather than affecting the half-life of the protein itself. In addition, a wash-out assay revealed that **AZ-9** has a longer degradation effect on CDK9 in HCT116 cells after rinsed with PBS to remove the drugs and allowed to grow in drug-free medium for an additional 24 h (Fig. 2K and L). In brief, **AZ-9** strongly chemically induces the degradation of CDK9 in HCT116 cells, and the effect is not dependent on endogenous cellular influences.

2.3. *AZ-9 exhibits high selectivity in the degradation of CDK9*

Next, we explored the structural factors and universality of **AZ-9**, respectively. As shown in Supporting Information Fig. S6A. The results of qRT-PCR indicated that **AZ-9** did not affect the transcription of CDK9 in HCT116 cells. However, AT7519, the ligand used in this degrader, significantly reduced the content of mRNA of CDK9. Surprisingly, we further proved that AT7519 had no significant effect on the content of CDK9 or Cyclin T1 in dose- or time-dependent manner, which excluded the influence of the ligand itself on CDK9 degradation (Fig. S6B−S6E). Furthermore, times-TOF Pro-label free proteomics was performed to verify the selectivity of **AZ-9** for CDK9 degradation. As shown in Fig. 3A. After treatment with **AZ-9**, the levels of major homologous cell cycle CDKs (CDK2, CDK4, and CDK6) exhibited no significant change in HCT116 cells, and similar results could still be verified using Western blot (Fig. 3B and Fig. S6F). The results of HTRF assay against CDK1/2/4/6/9 demonstrated the high degradation selectivity of **AZ-9** (Supporting Information Table S1). Moreover, we validated the degradation selectivity of **AZ-9** for CDK9 and Cyclin T1 in different cell lines (HT-29, DLD-1, RKO and MOLM-13). The results indicate that **AZ-9** selectively degrades CDK9 and Cyclin T1 in different types of cells but has no significant effect on CDK2, CDK4, or CDK6 (Fig. 3C−F and Fig. S6G−S6J), which proves the potential of **AZ-9** as a chemical tool for research on CDK9. The PROTAC **AT-PRO** was further synthesized to compare its degradation efficiency (Supporting Information Fig. S7). However, the effects of **AT-PRO** on CDK9 and Cyclin T1 contents are not as significant as those of **AZ-9**, and **AT-PRO** has no effect on the degradation of CDK2, CDK4, or CDK6 (Fig. 3G and Fig. S6K). In addition, compounds possessing other ligands of CDK9, named **SNS-HYT** and **205-HYT**, were obtained for evaluation (Fig. S7). The results revealed that **SNS-HYT** and **205-HYT** also exhibited significant degradation selectivity towards CDK9 and Cyclin T1 (Fig. 3H and I, Fig. S6L and

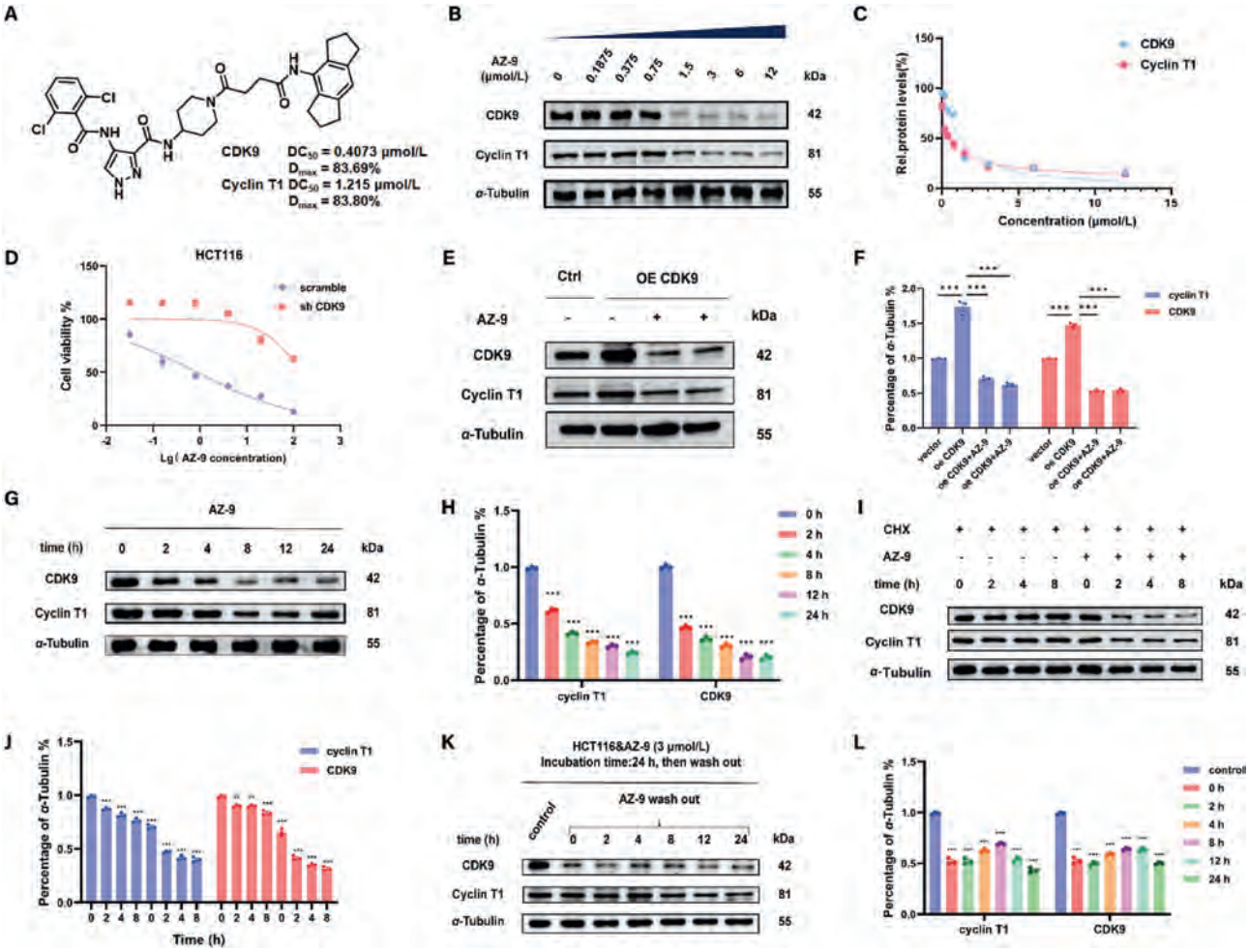

Figure 2 CDK9 degradation by **AZ-9** in HCT116 cells. (A) Structure of **AZ-9**; (B, C) Dose-dependent degradation of CDK9 and Cyclin T1 induced by **AZ-9**; (D) Cell viabilities of shCDK9 HCT116 cells and scramble control of **AZ-9**; (E, F) Degradation effects of **AZ-9** (1 μmol/L) in HCT116 cells and HCT116 cells with CDK9 overexpression; (G, H) Time-dependent degradation of CDK9 and Cyclin T1 induced by **AZ-9** (1 μmol/L); (I, J) CHX assay, CHX treated with or without **AZ-9** (1 μmol/L) for 8 h and the protein level indicated was monitored with immunoblot; (K, L) HCT116 cells were treated with **AZ-9** at 3 μmol/L for 24 h, followed by wash-out and incubation in compound-free medium at the indicated time point. The protein level indicated was monitored with immunoblot. The significance of the differences between vehicle group and administration groups was determined by one-way ANOVA test. Data are presented as mean ± SD; $n = 3$; $^{*}P < 0.05$; $^{**}P < 0.01$; $^{***}P < 0.001$; $^{****}P < 0.0001$; ns, not significant.

S6M), which confirms the universality of the active conservative combination of *S*-indacene and the length of the four atoms for the design of a selective CDK9 degrader.

*2.4. **AZ-9** promotes classic downstream pathway related to CDK9*

To confirm whether the downstream pathway effects induced by CDK9 degradation are consistent with the classical pathway effects induced by CDK9 inhibition. KEGG enrichment analysis of the proteomic data revealed that the protein levels of RNA polymerase-related pathways significantly changed (Fig. 4A). As shown in Fig. 4B−F. The level of RNA polymerase II phosphorylated at Ser 2 tended to significantly decrease, and the expression of three apoptosis-related genes (mRNAs) and proteins (Mcl-1, c-Myc and Bcl-2) also showed a synchronous downwards trend after treatment with **AZ-9**, together with the dose-dependent cleavage of caspase 3 and PARP (a substrate of caspase 3). Furthermore, a series of screens for assessing apoptotic phenotypes were performed to validate the effectiveness of **AZ-9**. Colony formation was performed to evaluate the effects of **AZ-9** on HCT116 cells. As shown in Supporting Information Fig. S8 and Supporting Information Fig. S11A−S11C, both **AZ-9** and AT7519 decreased the colony number in a dose-dependent manner. Moreover, the antiproliferative effects of **AZ-9** were better than those of AT7519 and **AT-PRO** at the same concentration. This result confirmed the *in vitro* antiproliferative effect of **AZ-9**. In addition, the results of the Annexin V-FITC/PI binding assay, GreenNuc living cell caspase 3 activity assay and TUNEL staining were used to investigate the mechanism of the cellular effects of **AZ-9** in the HCT116 cell line. As shown in Fig. S9 and Fig. S11D−S11F, the percentage of total apoptotic cells (Q3-UR + Q3-LR) increased in a dose-dependent manner. TUNEL staining also revealed that the number of cells that emitted red fluorescence (apoptotic cells) increased as the drug concentration increased (Supporting Information Fig. S12). Moreover, the activity of caspase 3 (a terminal

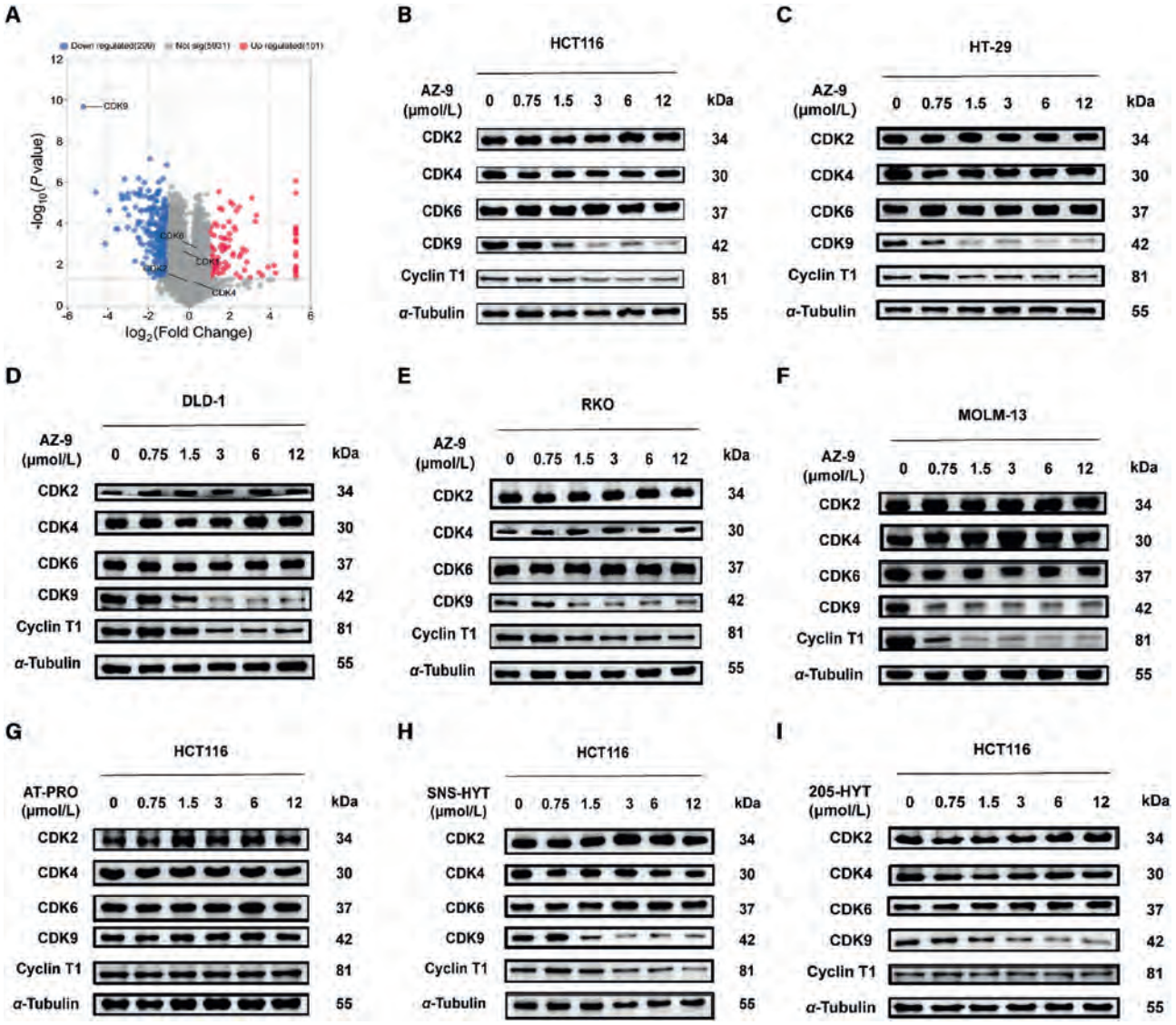

Figure 3 **AZ-9** is highly selective for CDK9 degradation. (A) Proteomic analysis of proteins differentially expressed in **AZ-9** (1 μmol/L)-treated HCT116 cells ($n = 3$). Volcano plots of the −log10 (*P* value) *versus* the log2 fold change. Proteins with −log10 (*P* value) > 2 (*P* value < 0.01) and log2 fold change >1 or < -1 were considered to have significantly changed in abundance. *P* values were calculated using two-tailed unpaired Student's *t*-test; (B−F) Dose-dependent changes in CDK2, CDK4, CDK6, CDK9 and Cyclin T1 expression induced by **AZ-9** in HCT116, HT-29, DLD-1, RKO, and MOLM-13 cells, respectively; (G−I) Dose-dependent changes in CDK2, CDK4, CDK6, CDK9 and Cyclin T1 expression induced by AT-PRO, SNS-HYT, and 205-HYT in HCT116 cells, respectively. The statistical charts were listed in Supporting Information Fig. S6. The significance of the differences between vehicle group and administration groups were determined by one-way ANOVA test. Data are presented as mean ± SD; $n = 3$; $^{*}P < 0.05$; $^{**}P < 0.01$; $^{***}P < 0.001$; $^{****}P < 0.0001$; ns, not significant.

marker of cell apoptosis) also tended to increase (Figs. S10 and S11G−S11I). The above phenotype results indicated the occurrence of caspase 3-mediated apoptosis.

2.5. *AZ-9 induced autophagy−lysosome pathway degradation of CDK9 by recruiting ATG101*

Encouraged by the above results. We were strongly interested in the degradation mechanism of CDK9 by **AZ-9** in HCT116 cells. First, the proteasome inhibitor MG132 and the lysosome inhibitor chloroquine (CQ) were used to confirm the subcellular localization of the degradation of CDK9 and Cyclin T1, and the results were shown in Fig. 5A and B, pretreatment with CQ significantly blocked CDK9 and Cyclin T1 degradation induced by **AZ-9** in HCT116 cells but not MG132, suggesting that engagement of the autophagy−lysosome pathway is essential for the observed CDK9 and Cyclin T1 degradation. Moreover, autophagy inhibitor 3-methyladenine (3-MA) did not exhibit potential effect on the degradation of CDK9 and Cyclin T1, which excluded the influence of autophagy caused by **AZ-9** itself. What' more, in the cell viability assay, only lysosome inhibitor CQ effectively reduced the decrease in cell viability caused by the degradation of CDK9 and Cyclin T1 induced by **AZ-9** (Fig. 5C). In addition, autophagosome-lysosome fusion inhibitor Bafilomycin A1 could also reverse CDK9 and Cyclin T1 degradation induced by **AZ-9** (Supporting Information Fig. S13). To explore the molecular mechanism of **AZ-9** induced autophagy−lysosome pathway

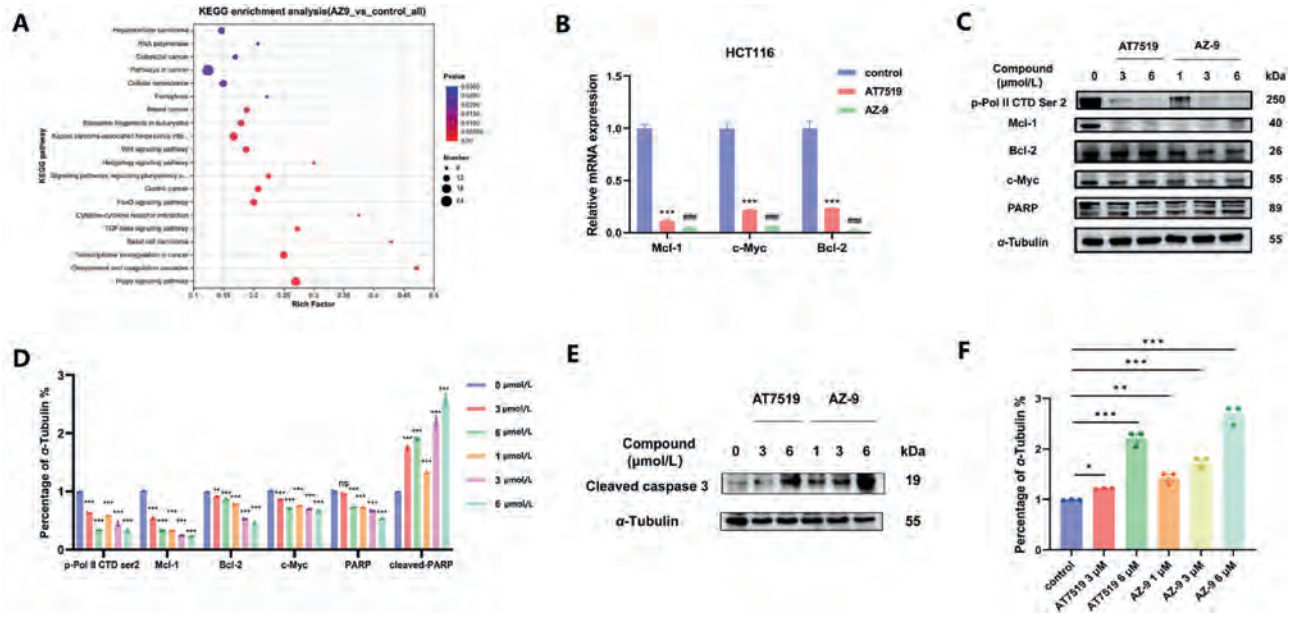

Figure 4 **AZ-9** promotes classical CDK9-related downstream pathways. (A) KEGG enrichment analysis of proteomics; (B) qRT-PCR analysis of Mcl-1, c-Myc and Bcl-2 in HCT116 cells after 24 h incubation of AT7519 (1 μmol/L) or **AZ-9** (1 μmol/L); (C, D) Regulation of **AZ-9** and AT7519 on phosphorylated RNA polymerase II (Ser 2) and the downstream signaling pathways of CDK9 in HCT116 cells after 48 h of incubation. (E, F) Regulation of **AZ-9** and AT7519 on cleaved caspase 3 in HCT116 cells after 48 h of incubation. The significance of the differences between vehicle group and administration groups were determined by one-way ANOVA test. Data are presented as mean ± SD; $n = 3$; $^{*}P < 0.05$; $^{**}P < 0.01$; $^{***}P < 0.001$; $^{****}P < 0.0001$; ns, not significant.

degradation of CDK9 and Cyclin T1, Co-Immunoprecipitation Mass Spectrum (Co-IP/MS) was used to identify proteins that interact with **AZ-9** and CDK9/Cyclin T1 complexes. And ATG101 was identified as a potential candidate (Fig. 5D), given that ATG101 is an essential component of the autophagy-initiating ULK complex in higher eukaryotes[32-33]. To verify this discovery, Co-immunoprecipitation was performed to evaluate the possible involvement of ATG101. After treatment with 1 μmol/L **AZ-9** for 48 h, we detected increased interactions between CDK9 and ATG101 (Fig. 5E), and an immunofluorescence colocalization assay confirmed these results (green fluorescence for CDK9 and red fluorescence for ATG101, Supporting Information Fig. S14). Moreover, we further explored the time and concentration dependence of the interaction between CDK9 and ATG101 under **AZ-9** intervention. As shown in Supporting Information Fig. S15, after treatment for 4 and 8 h, **AZ-9** could significantly enhance the interaction between CDK9 and ATG101 without showing a weakening trend (Supporting Information Figs. S15A and S16). When the administration concentration of **AZ-9** is 3 or 6 μmol/L, the protein interactions between CDK9 and ATG101 induced by chemistry remain stable (Fig. S15B and S15C). Meanwhile, **SNS-HYT** and **205-HYT** were used to verify the universality. As shown in Fig. S15D−S15I, CQ could still reverse the degradation effects of **SNS-HYT** and **205-HYT** on CDK9 and Cyclin T1 (Fig. S15D, S15E, S15G, S15H), and in co-IP experiments, the enhanced effects of **SNS-HYT** and **205-HYT** on the interaction between CDK9 and ATG101 could still be observed (Fig. S15F−S15I). Furthermore, in the ATG101-knockdown HCT116 cell model, the degradation effect of **AZ-9** on CDK9 and Cyclin T1 had been greatly weakened, which suggested that ATG101 is essential for maintaining the CDK9 degradation effect of **AZ-9** (Fig. 5F and G). However, in the cellular thermal shift assay (CETSA), **AZ-9** did not directly bind to ATG101 as demonstrated by an insignificant increase in the thermal stability of the target protein compared with that of the DMSO group (Fig. 5H). We further synthesized an *S*-indacene-biotin conjugate named **Ind-BIO** to explore whether the *S*-indacene moiety directly binds to ATG101 or ATG101-recruiting (Fig. 5I and J). The results indicated that **Ind-BIO** did not directly bind to ATG101 as well, suggesting that **AZ-9** enhances the interaction between CDK9 and ATG101 instead of binding to form a ternary complex, and the addition of **AZ-9** is relatively conservative in the recruitment process of CDK9 and ATG101, which might be one of the reasons why **AZ-9** can selectively degrade CDK9 and the partner protein Cyclin T1.

In addition, the key biomarker, LC3, which is involved in the degradation of the autophagy−lysosome pathway, was detected. As shown in Fig. 6A and B, the expression of LC3 mRNA was not affected by **AZ-9**. However, the ratio of LC3-II to LC3-I significantly increased after treatment with **AZ-9**, pretreatment with CQ significantly blocked the CDK9 degradation induced by **AZ-9** without affecting this ratio, and an immunofluorescence assay could also visually present the colocalization of LC3-II and CDK9 (green fluorescence for CDK9 and red fluorescence for LC3-II, Supporting Information Fig. S17) after treatment with **AZ-9**. Furthermore, in the mRFP-GFP-LC3 analysis, **AZ-9** significantly increased the number of GFP-mRFP^{+}(red) puncta, demonstrating an increase in the number of autolysosome (merge as yellow fluorescence, Fig. 6C). To visually observe the formation of autophagosomes, we observed the submicroscopic structure of **AZ-9**-treated HCT116 cells using a transmission electron microscopy (TEM). As shown in Fig. 6D, we could clearly observe the formation of autophagosomes (double arrow) and the process of fusion between autophagosomes and lysosomes (three arrows), together with precursor phagocytic vesicles with double layered membranes (single arrow). In brief, we preliminary demonstrated the process that **AZ-9** recruits ATG101 to initiate the autophagy−lysosome pathway and forms autophagosomes through

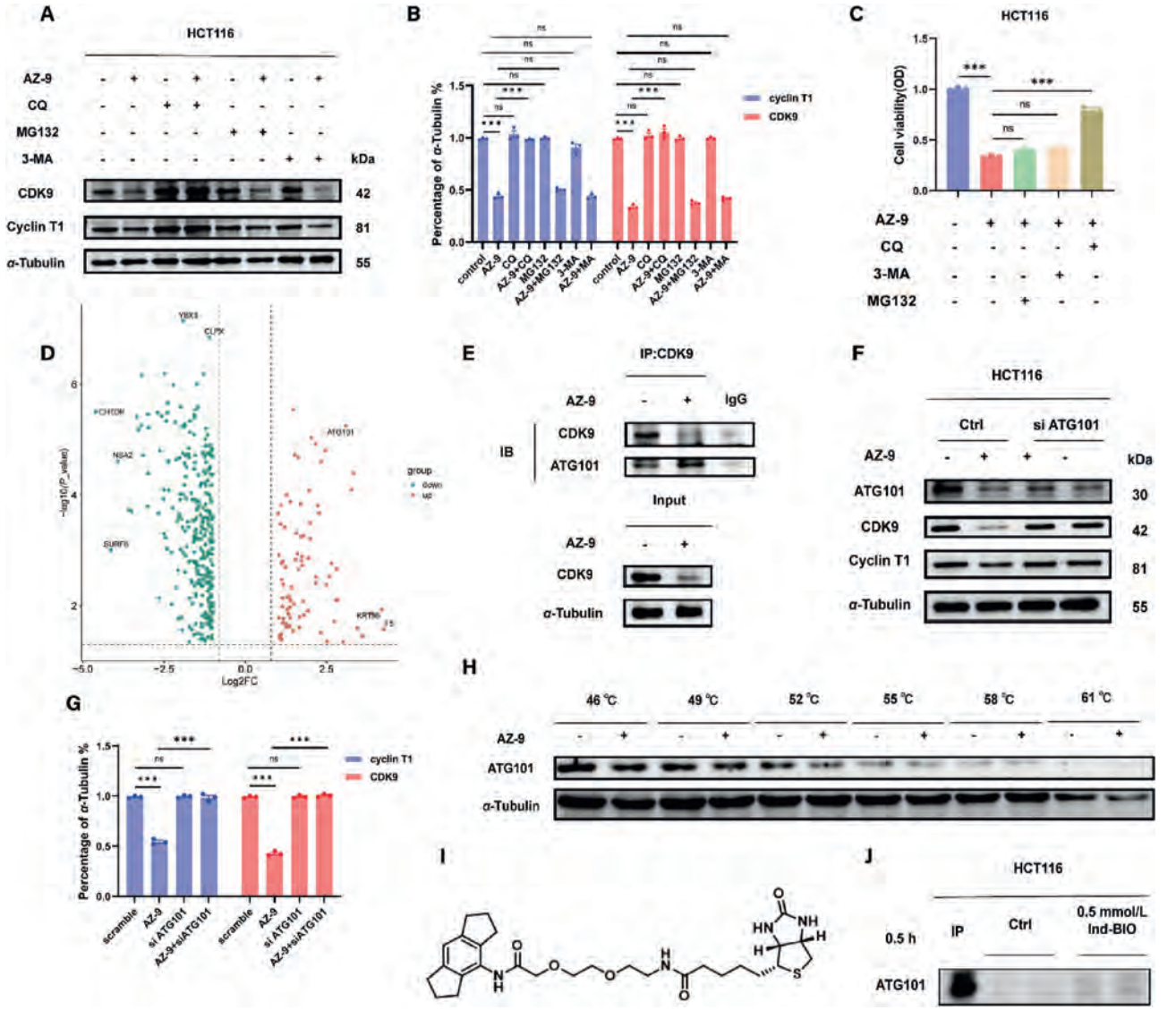

Figure 5 (A, B) HCT116 cells were pretreated with DMSO, CQ (2 μmol/L), MG132 (2 μmol/L), or 3-MA (2 μmol/L) for 8 h before treatment with **AZ-9** (1 μmol/L) for an additional 48 h, then promoting WB; (C) HCT116 cells were pretreated with DMSO, CQ (2 μmol/L), MG132 (2 μmol/L), or 3-MA (2 μmol/L) for 8 h before treatment with **AZ-9** (1 μmol/L) for an additional 48 h, then using CCK8 to test cells viability; (D) co-IP MS analysis of proteins differentially in **AZ-9** (1 μmol/L)-treated HCT116 cells ($n = 3$). Volcano plots of the −log10 (*P* value) *versus* the log2 fold change. Proteins with −log10 (*P* value) > 2 (*P* value < 0.01) and log2 fold change >1 or < -1 were considered to have significantly changed in abundance. *P* values were calculated using two-tailed unpaired Student's *t*-test; (E) HCT116 cells treated with 1 μmol/L **AZ-9** for 48 h were immunoprecipitated against ATG101. Then, Western blot was performed to assess the CDK9 and ATG101 levels; (F, G) Western blot of HCT116 cells and HCT116 cells treated with siATG101 on CDK9 and Cyclin T1 after treated with **AZ-9** (1 μmol/L); (H) Cellular thermal shift assay to evaluate the binding possibility of **AZ-9** (1 μmol/L) with ATG101 in HCT116 cells after incubation for 60 min; (I) Structure of Ind-BIO; (J) Western blot for target validation of *S*-indacene in protein extracts from HCT116 cells, and *S*-indacene was not found to bind directly with ATG101. The significance of the differences between vehicle group and administration groups were determined by one-way ANOVA test. Data are presented as mean ± SD; $n = 3$; $^{*}P < 0.05$; $^{**}P < 0.01$; $^{***}P < 0.001$; $^{****}P < 0.0001$; ns, not significant.

the recruitment and overexpression of LC3, which then fuses with lysosomes to degrade CDK9 and its partner protein Cyclin T1.

2.6. *AZ-9 shows significant CDK9 degradation and downstream pathway effects in HCT116 xenograft model*

Based on above information, the human liver microsomal stability assay and *in vivo* pharmacokinetic (PK) analysis of **AZ-9** were performed. As shown in Supporting Information Tables S2 and S3, **AZ-9** exhibited moderate metabolic stability with $t_{1/2}$ value of 25.3 min. PK analysis revealed that **AZ-9** possessed lower distribution in plasma, which might present specific organizational distribution characteristics. This results suggest that intraperitoneal injection may generate higher tumor treatment benefits. We further explored the antitumor capability in an HCT116 xenograft model. The mice were treated once daily for 15 days at the indicated doses and routes of administration, and AT7519 was selected as a compared control. As shown in Fig. 7A and B,

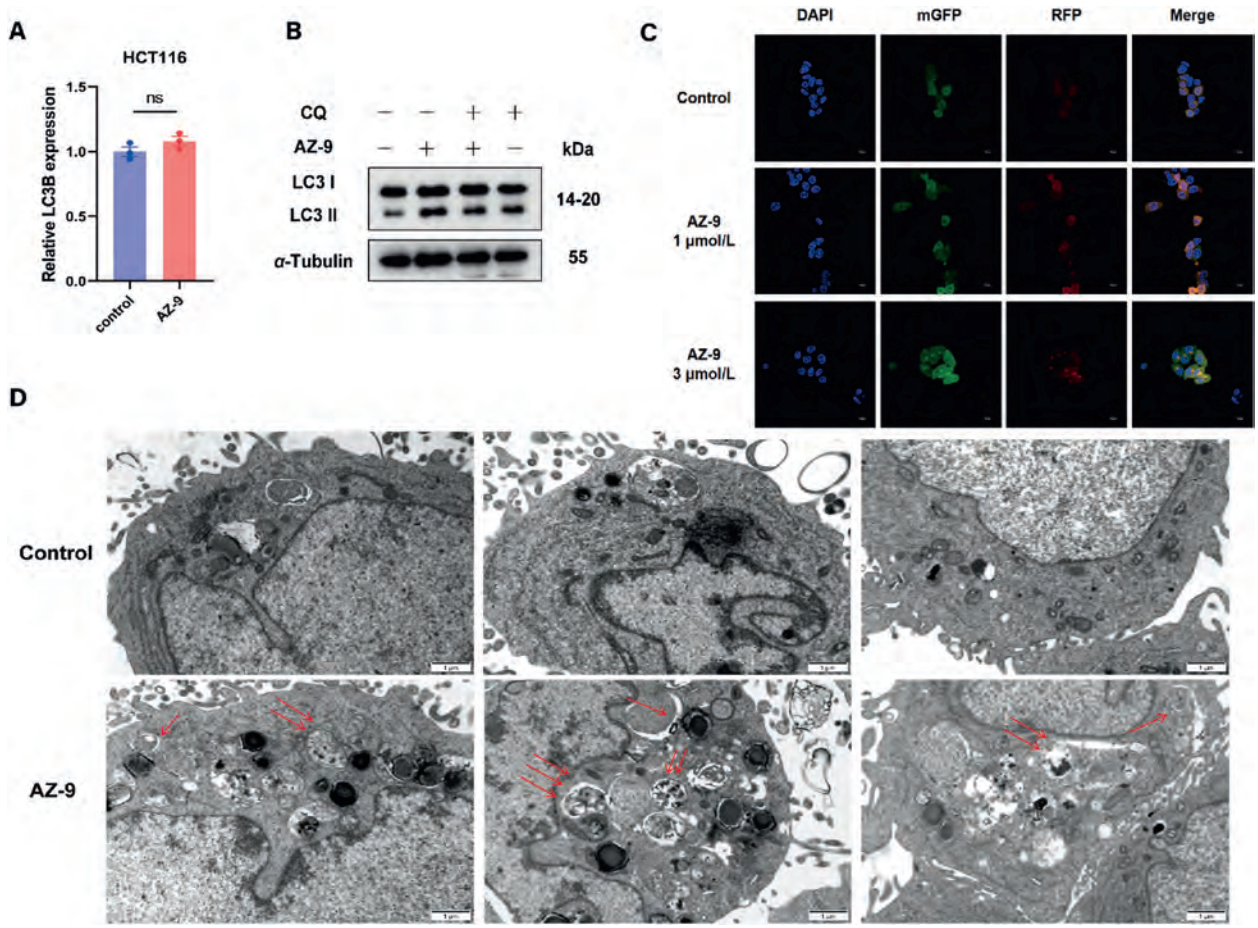

Figure 6 (A) qRT-PCR analysis of LC3 in HCT116 cells after 24 h incubation of **AZ-9** (1 μmol/L); (B) HCT116 cells were pretreated with DMSO, CQ (2 μmol/L) for 8 h before treatment with **AZ-9** (1 μmol/L) for an additional 48 h, then promoting WB to observe the expression changes of LC3I/II; (C) Expressing mRFP-GFP-LC3B in HCT116 cells were observed after treated with **AZ-9** (1 and 3 μmol/L). Scale bar = 10 μm; (D) Submicroscopic structure of HCT116 cells detected by TEM after treated with **AZ-9** 1 μmol/L, scale bar = 1 μm.

Supporting Information Fig. S18, both the positive control group and the **AZ-9**-treated group presented significantly reduced tumor volumes and weights. However, the use of AT7519 resulted in a weight loss in the test mice (Fig. 7C), which suggested the potential toxicity of AT7519 *in vivo*. Moreover, the results of western blotting and qRT-PCR assays in tumor tissues were similar to those at the cellular level. As illustrated in Fig. 7E and F, **AZ-9** also showed significant CDK9 and Cyclin T1 degradation effects and selectivity in HCT116 xenograft model. Moreover, **AZ-9** could inhibit the phosphorylation of RNA polymerase II at Ser 2 without any effects on RNA polymerase II, which resulted in the downregulated expression of apoptosis-related genes and protein. In addition, the cleaved of caspase 3 and PARP were also observed (Fig. 7D−G, H). Notably, compared with those in the vehicle and AT7519-treated groups, the number of Ki67-positive cells in the tumor xenograft treated with **AZ-9** was significantly lower (Supporting Information Fig. S19). Hematoxylin and eosin (H&E) staining revealed that the heart, liver, spleen, lungs, and kidneys had no obvious signs of toxicity in mice treated with **AZ-9** (Supporting Information Fig. S20). Overall, **AZ-9** could still demonstrate a significant degradation effect and selectivity of CDK9 and Cyclin T1 *in vivo*, together with effective intervention in related downstream effects and a reduction in the potential toxicity of the ligand itself *in vivo*.

3. Conclusions

In summary, we have developed the first ATG101-recruiting selective CDK9 degrader, **AZ-9**, for promoting autophagy−lysosome degradation. CDK9 and Cyclin T1 degradation induced by **AZ-9** is a dose- and time-dependent process, and **AZ-9** has high selectivity for CDK9 degradation without affecting cell cycle proteins (CDK2, CDK4, and CDK6). Moreover, the universality of CDK9 in different cell types degraded by **AZ-9** and the ligands used has also been fully validated. Further mechanistic studies revealed that the regulation of caspase 3-mediated apoptosis may contribute to the antiproliferative effects of **AZ-9** in the HCT116 cell line. For research on the degradation mechanism, we preliminarily confirmed that **AZ-9** recruits ATG101 to initiate the autophagy−lysosome pathway and forms autophagosomes through the recruitment of LC3, which fuses with lysosomes to degrade CDK9 and its partner protein Cyclin T1. Moreover, **AZ-9** has also been proven to exhibit good selective degradation of CDK9 and safety *in vivo*. As selective CDK9 degraders may have unparalleled advantages over conventional inhibitors in therapeutic treatment, our work provides a useful preliminary chemical tool to investigate CDK9-dependent biology and a promising method for potential therapy of tumors with high transcriptional dependency. Furthermore, for this novel

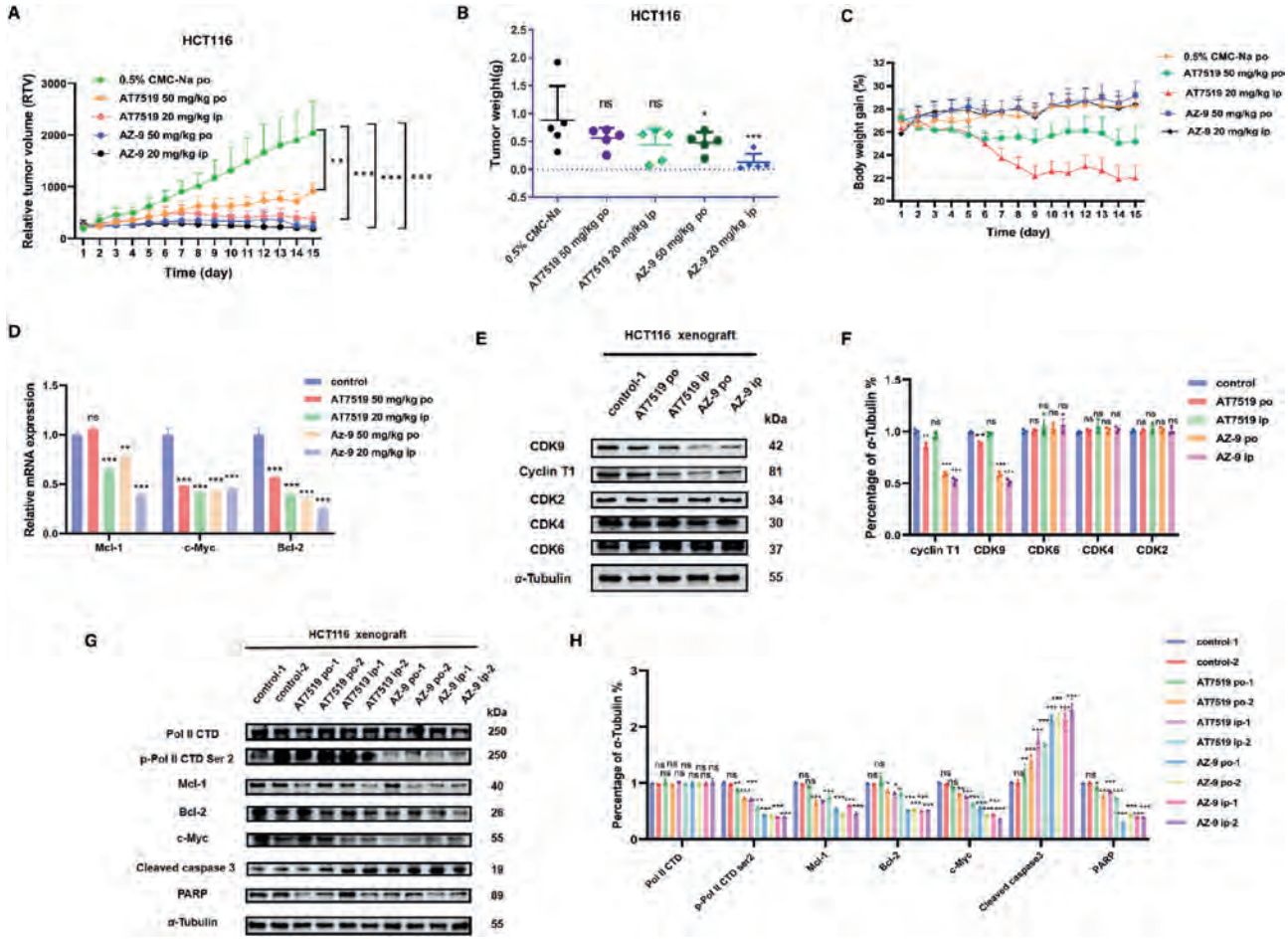

Figure 7 (A, B) Final tumour size and weight after treatment with **AZ-9** and AT7519 in HCT116 tumour-bearing mice; (C) The curves of mice weight during the treatment; The results are presented as mean ± SEM ($n = 5$). Significant difference is shown as $^{*}P < 0.05$, $^{**}P < 0.01$, ns, not significant by one-way ANVOA. (D) qRT-PCR analysis of mRNA expression of Mcl-1, c-Myc and Bcl-2 in tissue from HCT116 xenograft mouse model; (E, F) Regulation on CDK9, Cyclin T1, CDK2, CDK4, and CDK6 in tissue from HCT116 xenograft model; (G, H) Regulation on RNA polymerase II, phosphorylated RNA polymerase II and the downstream signal pathways of CDK9 in tissue from HCT116 xenograft mouse model. The significance of the differences between vehicle group and administration groups were determined by one-way ANOVA test. Data are presented as mean ± SD; $n = 3$; $^{*}P < 0.05$; $^{**}P < 0.01$; $^{***}P < 0.001$; $^{****}P < 0.0001$; ns, not significant.

hydrophobic-driven protein degradation strategy, we discovered and validated the existence of a non-proteasome degradation pathway for the first time, which might provide research ideas for chemical induction interventions for other types of pathogenic proteins.

4. Experimental

4.1. Chemistry

All the reagents (Energy Chemical, Shanghai, China) were used without further purification unless otherwise specified. Solvents were dried and redistilled prior to use in the usual manner. Analytical TLC was performed using silica gel HF254 (Qingdao Haiyang Chemical, Qingdao, Shandong, China). Preparative column chromatography was performed with silica gel H. Melting points were obtained on a Büchi melting point B-540 apparatus (Büchi Labortechnik, Flawil, Switzerland). ^{1}H and ^{13}C NMR spectra were recorded on a Bruker ARX 600 MHz spectrometer (Bruker, Zurich, Switzerland); ESI−MS were obtained by an Agilent 6120 SQ ESI−LC−MS instrument (Agilent, Santa Clara, CA, USA). HR-MS were obtained by a Bruker solariX HR-MS instrument (Bruker, Zurich, Switzerland). The purity of all target compounds was >95% as analyzed using a Waters high-performance liquid chromatography (HPLC), with the Agilent C18 column (4.6 mm × 250 mm, 5 μm), mobile phase: A = H_2O, B: methanol, and flow rate: 1 mL/min.

4.1.1. General procedure for the amide condensation reaction

To a solution of corresponding carboxylic acid (1 equiv.) in DMF, various corresponding amines (1.2 equiv.), EDCI (1.2 equiv.) and HOBt (1.2 equiv.) were added the mixture was stirred at room temperature for 8 h. After the reaction completed, the reaction mixture was extracted with DCM and the combined organic layer was dried over Na_2SO_4. The filtrate was concentrated purified by a silica gel column chromatography to afford target intermediates or compounds.

4.1.2. General procedure for the ester hydrolysis reaction

To a solution of corresponding methyl ester (1 equiv.) in MeOH, LiOH (10 equiv.) aqueous solution was added and the mixture was

stirred at 80 °C for 2 h. After the reaction completed, the pH of the mixture was adjusted to 3 with 1 mol/L HCl and filtrated to afford corresponding carboxylic acid, which was used in the next steps without any purification.

4.1.3. General procedure for the removal reaction of Boc

To a solution of corresponding intermediates in 4 mol/L HCl/EA, the mixture was stirred for 6 h. After the reaction completed monitored by TLC. The reaction mixture was concentrated. Slurried by EA and filtrated to afford corresponding amide intermediates, which were used in next steps (Supporting Information Schemes S1−S10).

4.2. Biological assays

4.2.1. Cell lines and cell culture

HCT116 (1640 + 10%FBS), HT-29 (Mccoy's 5A + 20%FBS), RKO (MEM+10%FBS), DLD-1 (1640 + 10%FBS), and MOLM-13 (1640 + 10% FBS) were from the Cell Bank of Chinese Academy of Sciences. Cell cultures were maintained at 37 °C in an incubator containing 5% carbon dioxide.

4.2.2. Cell cytotoxicity assay

Cytotoxicity of test compounds against HCT116 cells was evaluated using an CCK8 assay *in vitro*. Cells were seeded into 96-well plates at a density of 5×10^3 cells per well and stabilized at 37 °C with 5% CO_2 for 24 h. Compounds were added to each well at various concentrations and then the cells were incubated for 48 h. The CCK8 solution (10 μL 0.5 mg/mL) was added to each well, and the cells were incubated for another 4 h. Then the absorbance of samples was measured at 450 nm. The GI_{50} values were calculated according to Logit method after getting the inhibitory rate.

4.2.3. Cell colony formation assay

HCT116 cells were seeded into 6-well plates at 37 °C with 5% CO_2 for 24 h and then treated with compounds at various concentrations for 14 days. Then, cells were stained with crystal violet solution and clones' numbers were counted directly with naked eyes.

4.2.4. Annexin V/PI staining assay

Cells apoptosis was assessed using Annexin V/PI staining assay. HCT116 cells were seeded into 6-well plates for 24 h and then treated with compounds at various concentrations for 48 h. Then, cells were collected, washed with 500 μL annexin-binding buffer and stained with 5 μL annexin V-FITC and 5 μL PI for 15 min at 25 °C. After that, the samples were analyzed by flow cytometry (BD Accuri C6 Plus, CA, USA).

4.2.5. TUNEL staining

The slides were immersed in 4% paraformaldehyde (pH 7.4) for 25 min at room temperature and then washed with PBS 3 times. The cells were immersed in 0.1% Triton X-100 solution prepared with PBS for 10 min (operation on ice) and then washed twice with PBS. Dilute 5 × equilibration buffer with deionized water and 100 μL 1 × equilibration buffer was added to each climbing tablet to cover the sample area to be tested, then incubated at room temperature for 15 min. After the buffer solution of 1 μD was added to the buffer solution, most of the buffer solution was added to the buffer solution of 1 μD, and then the buffer solution was used to wash off the buffer. The slides were placed in a wet box and incubated at 37 °C for 60 min. The wet box was wrapped with aluminum foil to avoid light. They were then washed 3 times with PBS with DAPI dripped and incubated in dark for 5 min. The specimens were stained with nuclei. The water-absorbent paper was used to absorb the liquid on the climbing sheet, and the sealing liquid containing anti fluorescence quenching agent was used to seal the film, and then the images were observed and collected under the fluorescence microscope.

4.2.6. GreenNuc living cell caspase 3 activity assay

HCT116 cells were seeded at a density of 6×10^5 cells per well and treated with various concentrations of compounds for 48 h. Subsequently, the cells were incubated with GreenNuc™ caspase 3 substrate and finally analyzed by flow cytometry (BD Accuri C6 Plus, CA, USA).

4.2.7. qRT-PCR analysis

Total RNA was isolated using TRIzol reagent (Invitrogen Life Technologies, Carlsbad, CA, USA) and transcribed to cDNA using PrimeScript Master Mix Kit (Takara, Kyoto, Japan). After quantitation and diluting to 200 ng/μL with DEPC treated water, the cDNA was used as a template for PCR using the TB-Green Premix Ex Taq II kit (Takara, Kyoto, Japan) in a CFX Connect Real-Time System (Bio-rad, CA, USA). The primers used in this study are presented in Supporting Information Table S4. β-actin was selected as an internal control for each experiment. The cycling conditions were as follows: predenaturation at 95 °C for 30 s, followed by 40 cycles at 95 °C for 30 s, at 60 °C for 5 s, and at 60 °C for 30 s. The specificity of the amplification products was confirmed by a melting curve analysis. All reactions were run in triplicate. As a measure of relative change in expression between the parental and resistant samples, ΔΔCt values were calculated and converted to approximate fold change values ($2^{-\Delta\Delta Ct}$).

4.2.8. Western blotting assay

Cells in the logarithmic growth phase were seeded in 12-well culture plates, 5×10^5 cells per well, and cultured with 1 mL culture medium containing the corresponding concentrations of the compounds. After processing for the corresponding time, the cells were collected by centrifugation. Cells were washed twice with precooled PBS followed by centrifugation to remove PBS, 100 μL loading buffer was added, cells were resuspended, and samples were boiled and denatured at 100 °C for 10 min. Appropriate amounts of protein samples were subjected to Tricine-SDS-PAGE for electrophoresis. After electrophoresis, under steady flow conditions, the proteins were transferred to nitrocellulose membranes, followed by blocking, overnight incubation of the primary antibody at 4 °C, incubation of the secondary antibody in the next day, and finally exposure. Image Lab 6.0 was used to perform grayscale analysis.

4.2.9. Immunoprecipitation (IP)

Cell lysates were incubated overnight with the corresponding antibodies at 4 °C with gentle rotation. The next day, immunogen-antibody complexes were captured by incubation for 1 h with protein A/G magnetic beads (MedChemExpress, Shanghai, China) at 4 °C with gentle rotation. Then, beads were washed three times with wash buffer. The immunocomplexes were analyzed by WB.

4.2.10. Immunofluorescence staining

HCT116 cells were seeded in 12-well plates until reaching a confluency of approximately 70%. Subsequently, the cells were

treated with DMSO or different concentrations of compounds for 48 h. After the incubation period, the cells were washed 3 times with cold PBS and fixed with 4% paraformaldehyde for 10 min at room temperature. To permeabilize the cells, 0.2% Triton X-100 in PBS was applied for 5 min at room temperature. After that, the cells were blocked with 5% BSA (Sangon Biotech (Shanghai) Co., Ltd., A500023) in TBST for 0.5 h at room temperature. Primary antibodies were incubated at 4 °C overnight. After washing the cells 4 times with TBST, and the second antibodies were incubated for 1 h at room temperature. Finally, the nucleus was stained with 4,6-diamidino-2-phenylindole (DAPI, Invitrogen, R37606) and the images were observed and collected under the fluorescence microscope.

4.2.11. shRNA knockdown of CDK9

We screened two hairpin shRNAs targeting CDS (Coding sequence) of human CDK9 transcripts and found two independent sequences that reduced mRNA levels by>70%. These shRNAs were in the pLKO.1 vector (shCDK9-1 and shCDK9-2). Besides, a shRNA targeting 3′-UTR of human ACTL6A transcripts was constructed in the pLKO.1 vector (shCDK9). The targeting sequences used are shown as follows:

Sh CDK9-1: F-CCGGGCACAGTTTGGTCCGTTAGAACTCGAGTTCTAACGGACCAAACTGTGCTTTTTG.

Sh CDK9-1: R-AATTCAAAAAGCACAGTTTGGTCCGTTAGAACTCGAGTTCTAACGGACCAAACTGTGC.

Sh CDK9-2: F-CCGGCTACTACATCCACAGAAACAACTCGAGTTGTTTCTGTGGATGTAGTAGTTTTTG.

Sh CDK9-2: R-AATTCAAAAACTACTACATCCACAGAAACAACTCGAGTTGTTTCTGTGGATGTAGTAG.

To produce lentiviral particles, 2×10^5 HCT116 cells in a six-well plate were co-transfected with 8 μg pLKO.1 shRNA construct, 6 μg psPAX2, and 4 μg pMD2G. The supernatant containing viral particles was harvested at 48 h after transfection, and was filtered through Millex-GP Filter Unit (0.45 μm pore size, Millipore). To infect cancer cells with lentivirus, cells were infected twice with culture medium containing 2 mL lentivirus, 200 μL FBS and 5 mg/mL polybrene (Sigma) at 37 °C for 24 and 48 h. To increase the knockdown efficiency, infected cells were under several days of puromycin selection.

4.2.12. Overexpression of CDK9 in HCT116 cells

The plasmid (PGMLV-CMV-H_CDK9-3 × Flag-EF1-mScarlet-T2A-Puro) related to CDK9 overexpression in cells was purchased from Genogmeditech. The operation process was performed as previously described (shRNA knockdown of CDK9). The targeting sequences used are shown as follows:

GCCACCATGGCAAAGCAGTACGACTCGGTGGAGTGCCCTTTTTGTGATGAAGTTTCCAAATACGAGAAGCTCGCCAAGATCGGCCAAGGCACCTTCGGGGAGGTGTTCAAGGCCAGGCACCGCAAGACCGGCCAGAAGGTGGCTCTGAAGAAGGTGCTGATGGAAAACGAGAAGGAGGGGTTCCCCATTACAGCCTTGCGGGAGATCAAGATCCTTCAGCTTCTAAAACACGAGAATGTGGTCAACTTGATTGAGATTTGTCGAACCAAAGCTTCCCCCTATAACCGCTGCAAGGGTAGTATATACCTGGTGTTCGACTTCTGCGAGCATGACCTTGCTGGGCTGTTGAGCAATGTTTTGGTCAAGTTCACGCTGTCTGAGATCAAGAGGGTGATGCAGATGCTGCTTAACGGCCTCTACTACATCCACAGAAACAAGATCCTGCATAGGGACATGAAGGCTGCTAATGTGCTTATCACTCGTGATGGGGTCCTGAAGCTGGCAGACTTTGGGCTGGCCCGGGCCTTCAGCCTGGCCAAGAACAGCCAGCCCAACCGCTACACCAACCGTGTGGTGACACTCTGGTACCGGCCCCCGGAGCTGTTGCTCGGGGAGCGGGACTACGGCCCCCCCATTGACCTGTGGGGTGCTGGGTGCATCATGGCAGAGATGTGGACCCGCAGCCCCATCATGCAGGGCAACACGGAGCAGCACCAACTCGCCCTCATCAGTCAGCTCTGCGGCTCCATCACCCCTGAGGTGTGGCCAAACGTGGACAACTATGAGCTGTACGAAAAGCTGGAGCTGGTCAAGGGCCAGAAGCGGAAGGTGAAGGACAGGCTGAAGGCCTATGTGCGTGACCCATACGCACTGGACCTCATCGACAAGCTGCTGGTGCTGGACCCTGCCCAGCGCATCGACAGCGATGACGCCCTCAACCACGACTTCTTCTGGTCCGACCCCATGCCCTCCGACCTCAAGGGCATGCTCTCCACCCACCTGACGTCCATGTTCGAGTACTTGGCACCACCGCGCCGGAAGGGCAGCCAGATCACCCAGCAGTCCACCAACCAGAGTCGCAATCCCGCCACCACCAACCAGACGGAGTTTGAGCGCGTCTTC.

4.2.13. Cellular thermal shift assay (CETSA)

The HCT116 cells were lysed by seven repeated freeze−thaw cycles with liquid nitrogen, and protein concentrations were determined by BCA assay. Cell lysates (1 mg/mL) were treated with either DMSO vehicle or **AZ-9** for 1 h at 37 °C. Cell lysates were then separated into six fractions for thermal profiling. Fractions were heated at the indicated temperatures (46−61 °C) for 3 min using a thermal shaker (MB100-2A Thermal shaker, Allsheng), followed by 3 min at room temperature. Samples were then centrifuged at 20,000×*g* for 20 min to separate protein aggregates from soluble proteins. Supernatants were collected and analyzed by Western blotting.

4.2.14. Streptomycin magnetic bead enrichment experiment for ATG101

Ind-BIO(0.5 mmol/L)was incubated with proteins extracted from HCT116 cells, followed by affinity enrichment using streptavidin magnetic beads, and validated by western blotting with an ATG101 antibody.

4.2.15. Proteomics assay

TIMS-TOF Pro-label free proteomics were performed using SAPT, a fast and efficient approach for simultaneous profiling of protein N- and C-terminome methods[34]. HCT116 cells were seeded at 2×10^6 cells/3 mL in the 6 cm plates and treated with 0.1% DMSO or 500 nmol/L **AZ-9** for 6 h. Cells were harvested and washed three times with 1 × PBS. Then the cells were centrifuged at 2000 rpm for 5 min to collect cell pellets in a refrigerated microfuge and frozen at −80 °C until further analysis. Harvested HCT116 cells were dealt with as described[34]. Cell samples were first processed by peptide fractionation through an SCX-SPE Column. The cell samples were then subjected to peptide dimethylation and dmen-amidation. The last LC−MS/MS analysis of fraction samples were performed on a nano-HPLC chromatography system connected to a hybrid trapped ion mobility spectrometry quadrupole time-offlight mass spectrometer (TIMS-TOF Pro, Bruker Daltonics, Billerica, MA, USA) *via* a CaptiveSpray nanoelectrospray ion source[35].

4.2.16. siRNA transfection

ATG101 siRNA was obtained from Santa Cruz, and siRNA transfection was performed as described. Briefly, HCT116 cells were seeded onto a 6-well plate at a density of 0.6×10^6 cells/well. Once the cells reached 70%−80% confluence, they were transfected with either control siRNA or siRNA using Lipofectamine 3000 Transfection Reagent (Invitrogen) according to the manufacturer's instructions. After 48 h of transfection, the cells

were gently washed with PBS and then incubated in AE17-TCM supplemented with or without DM-αKG for 24 h. The cells were subsequently harvested for analysis of mRNA expression and metabolites.

Sequences:

hATG101-723 (GGAGAAGGUGGGUGAGAAATT, UUUCUCACCCACCUUCUCCTT);

hATG101-586 (GGGCAGAUGUCCUUGGAGUTT, ACUCCAAGGACAUCUGCCCTT);

hATG101-404 (GCAAGUUCCACUACAAGAATT, UUCUUGUAGUGGAACUUGCTT).

4.2.17. mRFP-GFP-LC3B staining analysis

HCT116 cells were seeded at a density of 5×10^5 cells per well and treated with various concentrations of compound **AZ-9** for 48 h. Adding 200 μL ENI.S (optimized culture medium) to each hole. Transfection begins after cell adhesion on the second day. Dilute the virus stock solution to a final concentration of 1×10^8 TU/mL using ENI-S (optimized culture medium), with 20 μL virus working solution per well. After incubating in an incubator for 24 h, replace with fresh culture medium and continue to cultivate for 72 h before using it for staining experiments.

4.2.18. In vivo antitumor assay

The experimental procedures of the animal study were approved by the Animal Care and Use Committee at Shenyang Pharmaceutical University (No. SYPU-SQ-001). HCT116 cells (5×10^6) were unilaterally injected into the armpit of 6 weeks old female BALB/c nu−nu mice (Shanghai SLAC Laboratory Animal Co., Ltd.). After 10 days of observation, mice that successfully modeled with HCT116 cells were randomly divided into four groups ($n = 6$) and received an oral or intraperitoneal injection administration, and CMC-Na as a negative control once every day for 2 weeks. Body weights and tumor sizes were determined every day. The tumor volume was measured by a vernier caliper and calculated using the following formula: 0.5 × short × short × long. At the end of the experiment, the mice were sacrificed, and the tumor tissues were weighed and used for PCR, WB, IHC and H&E-stained.

4.2.19. Molecular docking study

The CDK9 (PDB code: 4BCF) crystal structure was downloaded from protein data bank (https://www.rcsb.org/), and processed with the Protein Preparation Wizard in the Schrödinger suite. The protein structures were adjusted and modified, followed by adding hydrogen atoms, deleting solvent water molecules, and defining right bonds orders using Prime. The protonation and tautomeric states of Asp, Lys, and His were assigned at pH 7.4 state. Afterward, all hydrogen atoms of CDK9 complexes were optimized with OPLS_2005 force field, which minimized and converged heavy atoms to a RMSD of 0.3. The selected inhibitors were prepared by using LigPrep from the Schrödinger suite with the OPLS_2005 force field. The structures of inhibitors were also adjusted and modified, followed by adding all hydrogen atoms, checking the bond order and atom types. Receptor grids were generated before docking with the active site determined by the literature[36]. The prepared protein−ligand complex was imported into Glide 9.7, which was defined as the binding site. The size of the docking grid box was 20 Å × 20 Å × 20 Å. Based on the OPLS_2005 force field, the grid of CDK9 crystal structure was generated. The standard precision (SP) mode was set for docking studies without constrained binding to gain results.

4.2.20. Statistical analysis

Statistical analysis was carried out using an unpaired two-tailed Student's *t* test in GraphPad Prism 8. $*P < 0.05$; $**P < 0.01$; $***P < 0.001$, $****P < 0.0001$ and ns denotes not significant. *P* value < 0.05 was considered as significant.

Acknowledgments

This study was financially supported by Key R&D Program of Shandong Province, China (No. 2024CXPT028); National Natural Science Foundation of China (22177079, 22477085); National Natural Science Foundation of Shanghai Province, China (No. 24ZR1477400); National Natural Science Foundation of Shandong Province, China (No. ZR2024QC286); Taishan Scholar Foundation of Shandong Province (tstp0648, China).

Author contributions

Supervision: Yang Liu, Jia Li, Maosheng Cheng, and Yili Sun; Conceptualization & Methodology: Ye Zhong and Jing Xu; Validation & Investigation: Ye Zhong and Jing Xu; Formal analysis: Huiying Cao and Jie Gao; Writing - Original Draft: Ye Zhong and Jing Xu; Data Curation & Project administration: Shaoyue Ding, Zhaohui Ren and Huali Yang; Writing - Review & Editing: Yang Liu, Jia Li, and Maosheng Cheng.

Conflicts of interest

The authors declare no conflicts of interest.

Appendix A. Supporting information

Supporting information to this article can be found online at https://doi.org/10.1016/j.apsb.2025.03.047.

References

1. Chou J, Quigley DA, Robinson TM, Feng FY, Ashworth A. Transcription-associated cyclin-dependent kinases as targets and biomarkers for cancer therapy. *Cancer Discov* 2020;**10**:351−70.
2. Shen YL, Wang YM, Zhang YX, Ma SJ, Yang LH, Zhao CG, et al. Targeting cyclin-dependent kinase 9 in cancer therapy. *Acta Pharmacol Sin* 2022;**43**:1633−45.
3. Wu TZ, Qin Z, Tian YC, Wang JB, Xu CX, Li ZY, et al. Recent developments in the biology and medicinal chemistry of CDK9 inhibitors: an update. *J Med Chem* 2020;**63**:13228−57.
4. Hu C, Shen LJ, Zou FM, Wu Y, Wang BL, Wang AL, et al. Predicting and overcoming resistance to CDK9 inhibitors for cancer therapy. *Acta Pharm Sin B* 2023;**13**:3694−707.
5. Lücking U, Kosemund D, Böhnke N, Lienau P, Siemeister G, Denner K, et al. Changing for the better: discovery of the highly potent and selective CDK9 inhibitor VIP152 suitable for once weekly intravenous dosing for the treatment of cancer. *J Med Chem* 2021;**64**:11651−74.
6. Barlaam B, Casella R, Cidado J, Cook C, De Savi C, Dishington A, et al. Discovery of AZD4573, a potent and selective inhibitor of CDK9 that enables short duration of target engagement for the treatment of hematological malignancies. *J Med Chem* 2021;**63**:15564−90.
7. Freeman DB, Hopkins TD, Mikochik PJ, Vacca JP, Gao H, Naylor-Olsen A, et al. Discovery of KB-0742, a potent, selective, orally bioavailable small molecule inhibitor of CDK9 for MYC-dependent cancers. *J Med Chem* 2024;**66**:15629−47.

8. Santo L, Vallet S, Hideshima T, Cirstea D, Ikeda H, Pozzi S, et al. A novel small molecule multi-cyclin-dependent kinase inhibitor, induces apoptosis in multiple myeloma *via* GSK-3β activation and RNA polymerase II inhibition. *Oncogene* 2010;**29**:2325−36.
9. Chen R, Wierda WG, Chubb S, Hawtin RE, Fox JA, Keating MJ, et al. Mechanism of action of SNS-032, a novel cyclin-dependent kinase inhibitor, in chronic lymphocytic leukemia. *Blood* 2009;**113**:4637−45.
10. Cheng SS, Qu YQ, Wu J, Yang GJ, Liu H, Wang WH, et al. Inhibition of the CDK9−cyclin T1 protein−protein interaction as a new approach against triple-negative breast cancer. *Acta Pharm Sin B* 2022;**12**:1390−405.
11. Gao GP, Li JY, Cao Y, Li XD, Qian YQ, Wang XM, et al. Design, synthesis, and biological evaluation of novel 4,4′-bipyridine derivatives acting as CDK9−Cyclin T1 protein−protein interaction inhibitors against triple-negative breast cancer. *Eur J Med Chem* 2023; **261**:115858.
12. Chirnomas D, Hornberger KR, Crews CM. Protein degraders enter the clinic—a new approach to cancer therapy. *Nat Rev Clin Oncol* 2023; **20**:265−78.
13. Burslem GM, Crews CM. Proteolysis-targeting Chimeras as therapeutics and tools for biological discovery. *Cell* 2020;**181**:102−14.
14. Chamberlain PP, Hamann LG. Development of targeted protein degradation therapeutics. *Nat Chem Biol* 2019;**15**:937−44.
15. Li K, Crews CM. PROTACs: past, present and future. *Chem Soc Rev* 2022;**51**:5214−36.
16. Robb CM, Contreras JI, Kour S, Taylor MA, Abid M, Sonawane YA, et al. Chemically induced degradation of CDK9 by a proteolysis targeting chimera (PROTAC). *Chem Commun* 2017;**53**:7577−80.
17. King HM, Rana S, Kubica SP, Mallareddy JR, Kizhake S, Ezell EL, et al. Aminopyrazole based CDK9 PROTAC sensitizes pancreatic cancer cells to venetoclax. *Bioorg Med Chem Lett* 2021;**43**:128061.
18. Olson CM, Jiang BS, Erb MA, Liang YK, Doctor ZM, Zhang ZN, et al. Pharmacological perturbation of CDK9 using selective CDK9 inhibition or degradation. *Nat Chem Biol* 2018;**14**:163−70.
19. Pei J, Xiao YF, Liu XG, Hu WY, Sobh A, Yuan YX, et al. Piperlongumine conjugates induce targeted protein degradation. *Cell Chem Biol* 2023;**30**:203−13.
20. Bian JL, Ren J, Li YR, Wang JB, Xu X, Feng YF, et al. Discovery of Wogonin-based PROTACs against CDK9 and capable of achieving antitumor activity. *Bioorg Chem* 2018;**81**:373−81.
21. Qiu XQ, Li YQ, Yu B, Ren J, Huang HD, Wang M, et al. Discovery of selective CDK9 degraders with enhancing antiproliferative activity through PROTAC conversion. *Eur J Med Chem* 2021;**211**:113091.
22. Wei D, Wang HL, Zeng QH, Wang WJ, Hao BB, Feng XL, et al. Discovery of potent and selective CDK9 degraders for targeting transcription regulation in triple-negative breast cancer. *J Med Chem* 2021;**64**:14822−47.
23. Nie HJ, Li BF, Sun JY, Yuan YL, Zhang ZG, Hu H, et al. Discovery of a potent, selective and orally bioavailable CDK9 degrader for targeting transcription regulation in triple-negative breast cancer. *Bioorg Chem* 2024;**153**:107876.
24. Tokarski RJ, Sharpe CM, Huntsman AC, Mize BK, Ayinde OR, Stahl EH, et al. Bifunctional degraders of cyclin dependent kinase 9 (CDK9): probing the relationship between linker length, properties, and selective protein degradation. *Eur J Med Chem* 2023; **254**:115342.
25. Kastl JM, Davies G, Godsman E, Holdgate GA. Small-molecule degraders beyond PROTACs-challenges and opportunities. *SLAS Discovery* 2021;**26**:524−33.
26. Xie SW, Zhu JJ, Li JD, Zhan FY, Yao H, Xu JY, et al. Small-molecule hydrophobic tagging: a promising strategy of druglike technology for targeted protein degradation miniperspective. *J Med Chem* 2023;**66**: 10917−33.
27. He QD, Zhao XF, Wu DL, Jia SM, Liu CL, Cheng ZT, et al. Hydrophobic tag-based protein degradation: development, opportunity and challenge. *Eur J Med Chem* 2023;**260**:115741.
28. Xie SW, Zhan FY, Zhu JJ, Sun Y, Zhu HJ, Liu J, et al. Discovery of norbornene as a novel hydrophobic tag applied in protein degradation. *Angew Chem Int Ed Engl* 2023;**62**:e202217246.
29. Guo ML, He SP, Cheng JF, Li Y, Dong GQ, Sheng CQ. Hydrophobic tagging-induced degradation of PDEδ in colon cancer cells. *ACS Med Chem Lett* 2022;**13**:298−303.
30. Guo ML, Song YQ, Cheng JF, Dong GQ, Sun X, Sheng CQ. Hydrophobic tagging-induced degradation of NAMPT in leukemia cells. *Chin Chem Lett* 2024;**35**:109392.
31. Zhong Y, Xu J, Zhou RC, Tang L, Ding SY, Ren ZH, et al. Identification of a novel selective CDK9 inhibitor for the treatment of CRC: design, synthesis, and biological activity evaluation. *J Med Chem* 2024;**67**:4739−56.
32. Takahashi D, Arimoto H. Selective autophagy as the basis of autophagy-based degraders. *Cell Chem Biol* 2021;**28**:1061−71.
33. Mei LG, Chen XR, Wei FJ, Huang X, Liu L, Yao J, et al. Tethering ATG16L1 or LC3 induces targeted autophagic degradation of protein aggregates and mitochondria. *Autophagy* 2023;**19**:2997−3013.
34. Wang ZJ, Zhang L, Yuan WJ, Zhang Y, Lu HJ. SAPT, a fast and efficient approach for simultaneous profiling of protein N- and C-terminome. *Anal Chem* 2021;**93**:10553−60.
35. Wang Q, Liu Z, Wang KY, Wang Y, Ye ML. A new chromatographic approach to analyze methylproteome with enhanced lysine methylation identification performance. *Anal Chim Acta* 2019;**1068**:111−9.
36. Hole AL, Baumli S, Shao H, Shi SH, Huang SL, Pepper C, et al. Comparative structural and functional studies of 4-(thiazol-5-yl)-2-(phenylamino)pyrimidine-5-carbonitrile CDK9 inhibitors suggest the basis for isotype selectivity. *J Med Chem* 2013;**56**:660−70.